Supporting Information

Wulff *et al.* 10.1073/pnas.0813176106

SI Results

Analysis of Theta Rhythm in Relation to the Running Speed. Reduced theta oscillations during waking can arise either from slower running (1) and/or due to a defective theta generation independently of the running speed. To establish possible contribution of the two factors, we recorded LFP and the animal's position during exploration in an open field from additional 3 mutant and 3 control mice. The average running speed was similar in the two groups (6.8 ± 0.6, control, vs. 6.2 ± 0.1 cm/s, mutant, excluding immobility; note that theta power in the main data sample, Fig. 2*B*, is computed for detected theta during waking thus largely excluding immobility; 6.6 ± 0.7, control, vs. 5.8 ± 0.1 cm/s, including immobility). The regularity of running was similar between genotypes (0.10 ± 0.004, control, vs. 0.11 ± 0.021 cm/s^2, mutant, first derivative of the speed, including immobility; 0.11 ± 0.004, control, vs. 0.12 ± 0.022 cm/s^2, mutant, excluding immobility).

Theta rhythm amplitude (Hilbert transformed) and frequency (computed from interpeak intervals) were averaged within each of the 20 speed bins for each animal and pooled according to the genotype. Theta frequency was strongly associated with the running speed in control ($r = 0.7$, $P < 0.0001$, Spearman coefficient) but not in the mutant ($P \approx 0.3$). Theta amplitude was poorly correlated with the speed ($P > 0.1$ in either genotype) but displayed significant association in control mice when speed values <25 cm/s were considered ($r = 0.4$, $P < 0.01$). Alterations of theta oscillations between genotypes were clearly evident when similar values of the running speed were considered (Fig. S5, $P < 0.0001$, for theta amplitude, $F_{1,112} = 294$, and frequency, $F_{1,112} = 103$, ANCOVA could only be performed for significantly different regression slopes).

Analysis of Coupling After Adjustment for Attenuated Theta Rhythm in PV-Δγ2 Mice. We considered awake theta rhythm features that were associated with the modulation of concurrent gamma oscillations ($P < 0.1$). First, theta cycle amplitude reliably predicted modulation of gamma oscillation amplitude in control mice ($r = 0.6$, $P < 0.0001$ in control and p ≈ 0.8 in PV-Δγ2 mice). Amplitude modulation of gamma oscillations was reduced in mutants after adjustment for theta amplitude ($F_{1,59} = 65.4$, $P < 0.0001$, for small theta cycles, $F_{1,35} = 65.0$, $P < 0.0001$, for large theta cycles, ANCOVA, Fig. 4*D*; theta cycles of small and large amplitudes - theta to delta ratio <11 and ≥11 respectively - were treated separately to ensure equality of the regression slopes). Theta cycle amplitude also correlated with the modulation of gamma frequency ($r = 0.3$, $P < 0.05$ in control and $r = 0.4$, p ≈ 0.1 for PV-Δγ2 mice) but, again, did not explain its reduction in PV-Δγ2 mice ($F_{1,103} = 5.9$, $P < 0.05$). Second, although theta cycles of higher frequency displayed some association with a lower index of gamma amplitude modulation in mutants ($r = 0.1$, p ≈ 0.7 in control and $r = -0.2$, $P = 0.09$ in PV-Δγ2 mice), the adjusted group effect showed a significant difference between control and PV-Δγ2 mice ($F_{1,137} = 88.3$, $P < 0.0001$). Third, decreased variability of theta rhythm amplitude and frequency was associated with a stronger modulation of gamma amplitude ($r = -0.6$, $P < 0.0001$ and $r = -0.5$, $P < 0.001$ for theta amplitude and frequency respectively) and, to a smaller extent of gamma frequency ($r = -0.2$, $P \leq 0.05$ and p ≈ 0.1 for theta amplitude and frequency respectively) in control but not in PV-Δγ2 mice (p ≈ 0.1). The reduced coupling of theta and gamma oscillations was also evident after accounting for the stability of theta rhythm (gamma amplitude modulation: $F_{1,138} = 38.8$, $P < 0.0001$, $F_{1,117} = 18.4$, $P < 0.0001$ for theta amplitude and frequency normalized variances as covariates respectively).

SI Materials and Methods

Generation of PV-Δγ2 Mice. In γ2I77lox mice exon 4 of the γ2 subunit gene is flanked by loxP sites (2). In addition a codon was changed in exon 4, resulting in a neutral amino acid substitution (F77 to I) (2). Mice homozygous for the γ2I77lox gene were crossed with mice heterozygous for γ2I77lox and hemizygous for a PVCre transgene (3). Littermates of the following genotypes were used for the experiments: γ2I77lox/γ2I77lox/PVCre (PV-Δγ2) and γ2I77lox/γ2I77lox (littermate controls). Mice were genotyped by PCR analysis of genomic DNA from tail biopsies using the following primer pairs: γ2lx5′_s (5′-GTCATGCTAAATATCCTACAGTGG-3′) and γ2lx5′_as (5′-GGATAGTGCA-TCAGCAGACAATAG-3′) to test for the γ2I77lox allele (213-bp band for WT, 250-bp band for γ2I77lox), Cre1 (5′-GACCAGGTTCGTTCACTCATGG-3′) and Cre2 (5′-AGGCTAAGTGCCTTCTCTACAC-3′) to test for the Cre recombinase transgene (250-bp band for PVCre).

In Situ Hybridization. In situ hybridization with 35S-labeled oligonucleotide probes was as described in ref. 4. The oligonucleotide sequences were:

Parvalbumin (PV):
5′-TCTTCAGGCCCACCATCTGGAA-GAACTTTTTGTGGTCGAAGGAGT-3′,

$GABA_A$ receptor γ1 subunit:
5′-ATGCAAGGTTCCGTATTCCATGAGTGCT-GCAAACACAAAAATGAA-3′,

$GABA_A$ receptor γ2 subunit (Ex4):
5′-GTGTCTGGAATCCAGATTTTCCCCAC-CATATTGCTATTCAAC-3′,

$GABA_A$ receptor γ3 subunit:
5′-AGAGGGTGCTTGAAGGCTTATTCGAT-CAGGAATCCATCTTGTTGA-3′.

Images were generated from 4 to 12 week exposures to Biomax MR X-ray film (Eastman Kodak). To assess nonspecific labeling of the sections, each labeled oligonucleotide was hybridized to brain sections with a 100-fold excess of unlabeled oligonucleotide.

Immunohistochemistry. Adult animals were transcardially perfused with 4% paraformaldehyde in PBS, pH 7.4, brains were removed and 60-μm-thick sagittal or coronal sections were obtained using a Leica VT1000S vibratome. Free-floating sections were washed in PBS 3 times for 10 min, endogenous peroxidase activity was reduced in PBS plus 0.5% H_2O_2 for 10 min. After washing twice in PBS (10 min each), sections were permeabilized and blocked in PBS plus 0.3% Triton X-100 and 2% normal goat serum for 30 min at room temperature and subsequently incubated with anti-parvalbumin (rabbit polyclonal, 1/1000 dilution, Swant) primary antibody in a solution composed of 2% NGS, 0.3% Triton X-100 in PBS for 24 h at 4 °C. Incubated slices were washed 3 times in PBS plus 0.1% Triton X-100 for 10 min at room temperature, incubated for 1 h at room temperature with a 1:500 dilution of biotinylated goat anti rabbit IgG (Vector Laboratories) in PBS plus 0.1% Triton X-100, and subsequently washed twice in PBS plus 0.1% Triton X-100 and twice in PBS alone for 10 min at room temperature. DAB stainings were performed using an avidin-biotin kit (Vectastain Elite ABC Kit, Vector Laboratories). Slices were rinsed briefly

in Tris·HCl 10 mM, mounted on slides, dehydrated, rinsed in Xylol and coverslipped using Eukitt (Sigma–Aldrich).

For quantification of PV-positive hippocampal interneurons cells were counted (blind to the genotype) under a light microscope in DAB stained serial coronal sections matched for rostrocaudal level by bregma distance in PV-$\Delta\gamma 2$ mice and littermate controls. The total number of parvalbumin positive cells per hippocampus was counted. 3 mice of each genotype (4 to 12 hippocampi per mouse) were analyzed. The numbers of parvalbumin positive cells per hippocampus were averaged for each mouse. Average cell numbers were then calculated for each genotype and compared using unpaired Student's t test.

Whole-Cell Recordings. Transverse hippocampal slices (300 μm thickness) were cut from brains of 40- to 105-day-old mice using a vibratome (DTK-1000, Dosaka). Patch pipettes were pulled from borosilicate glass tubing (2 mm outer diameter, 1 mm wall thickness). When filled with intracellular solution, the resistance was 2.2 - 3.5 MΩ. Whole - cell recordings were obtained from basket cells and principal cells in the CA1 hippocampal subfield under visual control using infrared differential interference contrast videomicroscopy (5, 6). Basket cells had somata located in the CA1 principal cell layer or Compound IPSCs were evoked by a glass stimulation pipette (≈2-μm tip diameter) placed in the principal cell layer with a stimulation frequency of 0.2 Hz. Pulses were delivered by using a stimulus isolator and had an amplitude of 3 - 20 V and a duration of 200 μs. To obtain sequential recordings of compound IPSCs in basket cells and principal cells of the same slice preparation, first a basket cell recording was performed. The patch pipette was withdrawn and a subsequent principal cell recording was obtained under identical extracellular stimulation conditions. Somata of both, basket cell and principal neuron, were located in the same depth of the slice preparation. The recording temperature was 31 - 34 °C.

Multiclamp 700B amplifier (Axon Instruments) was used for current clamp and voltage clamp recordings. Basket cell recordings with initial resting potentials more positive than −55 mV and principal cell recordings with initial resting potentials more positive than −65 mV were discarded. At the beginning of the recording basket cells were identified on the basis of their spiking pattern at 1 s depolarizing current injections. Basket cells generated high frequency trains of nonaccommodating action potentials (mean action potential frequency 163 ± 9 Hz at 800 pA, $n = 6$ basket cell recordings in CA1). Posthoc morphological analysis revealed axonal arborizations in the principal cell layer (7). Biocytin-filled neurons were visualized with avidin-biotinylated peroxidase complex and 3,3-diaminobenzidine as chromogen (8). To record compound IPSCs, cells were held in the voltage-clamp mode (holding potential −70 mV) with series resistance (R_S) compensation (65 - 90%, lag 20 μs; R_S before compensation 8 - 15 MΩ). The stationarity of the series resistance in the postsynaptic neuron was assessed from the amplitude of the capacitive current in response to a 10 mV pulse, and the compensation was readjusted during the experiment when necessary. Compound IPSCs were filtered at 6 kHz using the 4-pole low-pass Bessel filter of the amplifiers and were digitized at 20 kHz using a 1401plus laboratory interface (Cambridge Electronic Design) interfaced to a Pentium-PC. Igor-based programs (Fpulse; homemade) were used for stimulus generation and data acquisition.

Solutions. The physiological extracellular solution contained 125 mM NaCl, 25 mM $NaHCO_3$, 25 mM glucose, 2.5 mM KCl, 1.25 mM NaH_2PO_4, 2 mM $CaCl_2$, and 1 mM $MgCl_2$ (bubbled with 95% O_2/5% CO_2 gas mixture). 10 μM 6-cyano-7-nitroquinoxaline-2,3-dione (CNQX) was added to the bath solution to block excitatory postsynaptic currents and 1 μM CGP55845A (Tocris) to block $GABA_B$ receptor-mediated currents. Pipettes used for extracellular stimulation of presynaptic axons contained Hepes-buffered Na^+-rich solution (ph = 7.2) (KOH, 308 - 315 mOsm). To verify that IPSCs were mediated by $GABA_A$ receptors, we further added 20 μM bicuculline methiodide to the extracellular solution in a subset of experiments ($n = 3$). The intracellular solution contained 110 mM K-gluconate and 40 mM KCl, 0.1 mM EGTA, 2 mM $MgCl_2$, 2 mM Na_2ATP, and 10 mM Hepes; the pH was adjusted to 7.2 with KOH; the osmolarity was 290–310 mOsm; 0.2 biocytin was added for intracellular labeling. Bicuculline methiodide was purchased from Sigma, CNQX from Tocris. Other chemicals were from Merck, Sigma, Riedel-de Haen or Gerbu.

Data Analysis. The peak current was determined from average traces as the maximum within a window of 2 - 6 msec duration following the stimulus artifact from the preceding baseline. The decay phase of compound IPSCs was fitted with a single exponential [$A \exp(-t/\tau_m)$] or with the sum of 2 exponentials [$A \exp(-t/\tau_1) + B \exp(-t/\tau_2)$], using a nonlinear least-squares fit algorithm; time constants are reported as single exponential (τ_m) or as amplitude-weighted mean [$\tau_w = (A\tau_1 + B\tau_2)/(A+B)$]. Values are given as mean ± SEM. Error bars in Figures also indicate SEMs. Significance of differences was assessed by a Mann–Whitney test at the significance level (p) indicated.

In Vivo Recordings

Implantation of Electrodes. Custom-made microdrives were loaded with independently movable tetrodes (fabricated from 12-μm stainless steel wires, Kanthal, Mörfelden-Walldorf, Germany), linear silicon probes (100-μm intersite distance, Acreo AB, Kista, Sweden) or arrays of single tungsten wires (40 μm, California Fine Wire Company, Grover Beach, CA, USA). Electrodes were implanted under isoflurane anesthesia above hippocampus (AP: 1.8, L(right):1, V: 0.7 mm) of control ($n = 13$) and PV-$\Delta\gamma 2$ ($n = 12$) mice. Neocortical electroencephalogram (EEG) and reference electrodes were miniature stainless-steel screws in the skull. Electromyogram (EMG) electrodes were inserted in the neck muscle. Implanted electrodes and microdrive were secured on the skull with dental acrylic.

Data Acquisition. Electrodes were connected to operational amplifiers (Noted B.T., Pecs, Hungary) to eliminate cable movement artefacts. Electrophysiological signals were differentially amplified, band-pass filtered (1 Hz - 10 kHz, MCP Plus signal conditioner, Alpha Omega, Nazareth, Israel) and acquired continuously at 20 kHz (Alpha-Map, Alpha Omega). Electrodes were positioned in the CA1 str. pyramidale using depth profile of ripple oscillations and unitary activity as a reference. Recordings were performed during exploratory behavior (foraging in an open field), awake immobility and sleep. Two light-emitting diodes were attached to the headset to track animal's position (in indicated experiments).

Data Analysis. Signal processing was carried out off-line by custom-written MATLAB (Mathworks) and occasionally by C++ algorithms. EEG was obtained by low-pass filtering and down-sampling of the wide-band signal to 1250 Hz. Recordings used for further analyses were selected based on the following criteria: the location of the electrode in str. pyramidale was judged by the maximal amplitude of ripples and multiunit activity in the wide-band signal. Smaller, slower (50–100 ms) potentials often concurring with ripples had to be equal in positive and negative directions. In these recordings vigilance states (waking, slow-wave sleep, SWS, and paradoxical sleep, PS) were reconstructed with 10 s resolution similarly as reported elsewhere (9). Waking (desynchronized neocortical EEG and phasic activity in the EMG, thus largely active waking), SWS (slow-wave activity in the neocortical EEG and decreased mus-

cle tone) and PS (desynchronized neocortical EEG and muscle atonia) were defined on the basis of neocortical EEG and EMG activity with a reference to neocortical EEG spectral density in the 0.8−4 Hz band (see Fig. S4). Epochs with ambiguous characteristics were marked on the hypnogram and not used for further analysis. The instantaneous running speed was computed from the mouse's position in an open field. For correlative analysis the running speed and LFP variables were first averaged for consecutive 0.5 second intervals and then for each speed bin (20 bins).

Theta oscillation epochs were manually selected during waking and PS. In this signal theta oscillations were further automatically detected based on theta-delta power ratio of at least 6. Power spectral density was computed with the multitaper method (NW = 3, window length 1024). Peaks of theta and of concurrent gamma oscillations were detected in 5–10 Hz and 35–85 Hz band-pass filtered signals. Amplitudes of the peaks and interpeak intervals were computed. For the analysis of coupling between theta and gamma oscillations positive peaks and interpeak intervals in the gamma band were assigned phase of the concurrent theta oscillation (obtained by Hilbert transform in 5–10 Hz band). Coefficient of modulation was estimated from resulting phase histograms by:

$$Q := r\,\frac{G_{\max} - G_{\min}}{G_{\max} + G_{\min}}\cos\left(\frac{|\Delta\theta p|}{2}\right)\sin\left(\frac{|\Delta\theta t|}{2}\right)$$

where $G_{\max}$ and $G_{\min}$ are the maximal and minimal gamma peak amplitudes (respectively, gamma instantaneous frequency) within the theta cycle; $\Delta\theta p$ is the phase lag between theta peak and actual phase distribution peak; $\Delta\theta t$ is the half-period of the empirical phase distribution; r, coefficient of determination for the fitted sine distribution. This estimation allowed for the joint quantification of theta—modulation depth and theta—periodicity of the gamma oscillation features.

Action potentials were detected in a band-pass filtered signal (0.8 Hz-5 kHz). Events with the magnitude exceeding 3 SD above mean were detected, spike waveforms were extracted and represented by the first 3 principle components (10). Spike sorting was performed automatically (KlustaKwik, see ref. 11) followed by manual clusters adjustment (Klusters, see ref. 12). Putative pyramidal cells were identified from their autocorrelograms (see Fig. 2D), firing rates <3 Hz and action potential width (10, 13). Single pyramidal cells with clear refractory period (< = 2 ms) were used in further analysis. The quality of sorted units was further estimated by computing the isolation distance of clusters (11) and database redundancy measures. The latter excluded possibly repeatedly recorded units in sequential recordings from the same tetrode based on the similarity of the spike waveform across tetrode channels.

The modulation of the unitary discharge by theta and gamma oscillations was computed for automatically (as above) detected theta epochs. Oscillation phase was extracted by the linear interpolation between wave peaks and troughs at 1250 Hz for theta and at 10 kHz for gamma oscillations. Phase histograms of individual spike trains were obtained and normalized, first, by the deviation (if any) of the underlying phase distribution from uniformity in respective phase bins and, second, by the total number of events. Individual unit histograms were convolved with the Gaussian kernel (10).

Coupling between theta and gamma rhythmicity in spike trains was further estimated by computing gamma-phase dispersion and gamma-band interspike intervals in theta-phase bins using bivariate series of gamma- vs. theta-phase and spike time vs. spike theta-phase respectively. The difference between 1 and the gamma-phase dispersion delivers gamma modulation depth of the discharge for each theta-phase bin for each unit. Theta modulation was estimated similarly to the LFP-gamma modulation with an adaptation for unitary (more variable along with generally lower number of events than in LFP analysis) data: only proper modulation depth was computed (division of the difference of maximal and minimal count by their sum).

Histology. After completion of the experiments, mice were deeply anesthetized, perfused intracardially with 4% PFA solution and decapitated. Brains were fixed in 30% formalin-sucrose. The brains where subsequently frozen, cut in 40-μm slices, stained with cresyl violet and recording sites were confirmed.

Statistical Analysis. Two-way ANOVA was used to estimate the significance of genotype- and vigilance state-related differences. The statistical significance of single comparisons was determined by the Wilcoxon rank sum test or t test depending on the distribution normality (determined by the Lillieforce test). The differences in the coupling of theta and gamma oscillations were further estimated with ANCOVA using theta - rhythm features as covariates. Circular statistics was performed using the Reyleigh test. P-values <0.05 were considered to indicate significance.

1. Czurkó A, Hirase H, Csicsvari J, Buzsáki G (1999) Sustained activation of hippocampal pyramidal cells by 'space clamping' in a running wheel. *Eur J Neurosci* 11:344–352.
2. Wulff P, *et al.* (2007) From synapse to behavior: Rapid modulation of defined neuronal types with engineered GABAA receptors. *Nat Neurosci* 10:923–929.
3. Fuchs EC, *et al.* (2007) Recruitment of parvalbumin-positive interneurons determines hippocampal function and associated behavior. *Neuron* 53:591–604.
4. Wisden W, Laurie DJ, Monyer H, Seeburg PH (1992) The distribution of 13 GABAA receptor subunit mRNAs in the rat brain. I. Telencephalon, diencephalon, mesencephalon. *J Neurosci* 12:1040–1062.
5. Stuart GJ, Dodt HU, Sakmann B (1993) Patch-clamp recordings from the soma and dendrites of neurons in brain slices using infrared video microscopy. *Pflugers Arch* 423:511–518.
6. Koh DS, Geiger JR, Jonas P, Sakmann B (1995) Ca(2+)-permeable AMPA and NMDA receptor channels in basket cells of rat hippocampal dentate gyrus. *J Physiol* 485 (Pt 2):383–402.
7. Buhl EH, Halasy K, Somogyi P (1994) Diverse sources of hippocampal unitary inhibitory postsynaptic potentials and the number of synaptic release sites. *Nature* 368:823–828.
8. Bartos M, Vida I, Frotscher M, Geiger JR, Jonas P (2001) Rapid signaling at inhibitory synapses in a dentate gyrus interneuron network. *J Neurosci* 21:2687–2698.
9. Parmentier R, Ohtsu H, Djebbara-Hannas Z, Valatx JL, Watanabe T, Lin JS (2002) Anatomical, physiological, and pharmacological characteristics of histidine decarboxylase knock-out mice: Evidence for the role of brain histamine in behavioral and sleep–wake control. *J Neurosci* 22:7695–7711.
10. Csicsvari J, Hirase H, Czurko A, Mamiya A, Buzsaki G (1999) Oscillatory coupling of hippocampal pyramidal cells and interneurons in the behaving Rat. *J Neurosci* 19:274–287.
11. Harris KD, Henze DA, Csicsvari J, Hirase H, Buzsaki G (2000) Accuracy of tetrode spike separation as determined by simultaneous intracellular and extracellular measurements. *J Neurophysiol* 84:401–414.
12. Hazan L, Zugaro M, Buzsaki G (2006) Klusters, NeuroScope, NDManager: A free software suite for neurophysiological data processing and visualization. *J Neurosci Methods* 155:207–216.
13. Henze DA, Borhegyi Z, Csicsvari J, Mamiya A, Harris KD, Buzsáki G (2000) Intracellular features predicted by extracellular recordings in the hippocampus in vivo. *J Neurophysiol* 84:390–400.

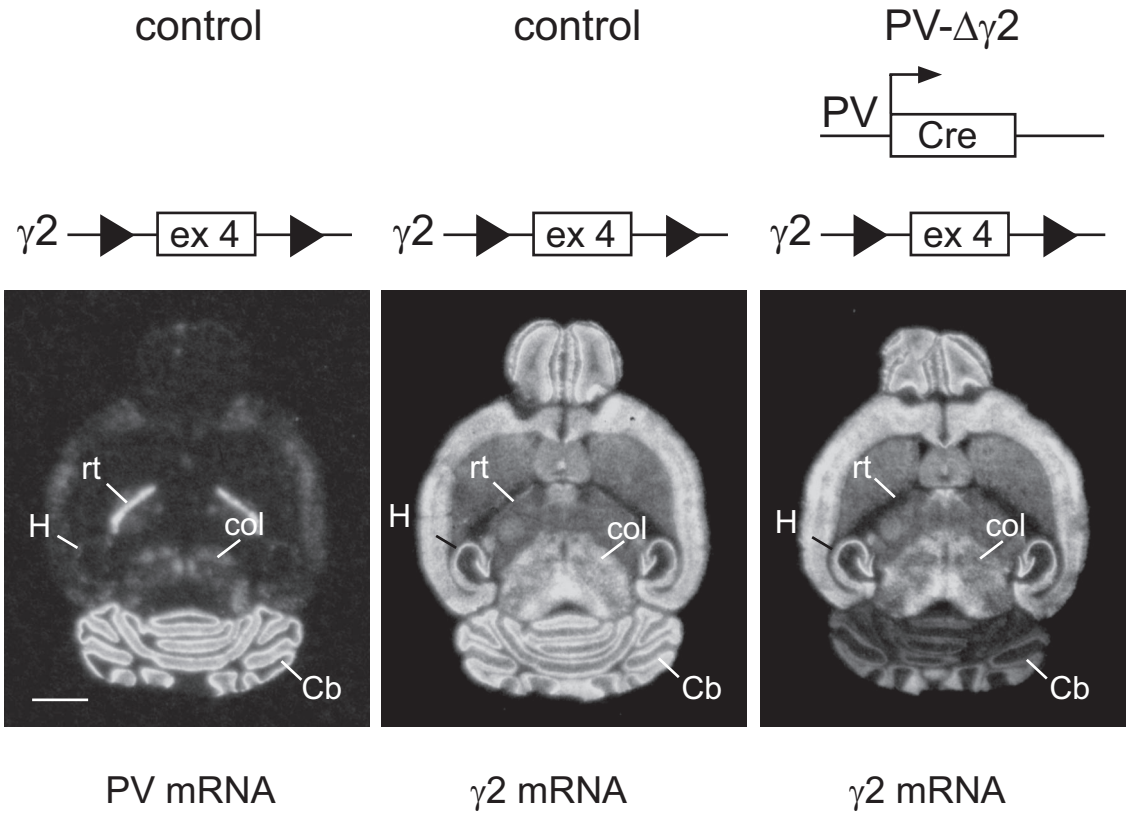

Fig. S1. $GABA_A$ receptor γ2 subunit gene epression in PV-Δγ2 mice. In situ hybridization (X-ray film) autoradiographs showing the expression of parvalbumin (left panel) and γ2 (middle and right panel) mRNA in brain sections from adult control (left and middle panel) and PV-Δγ2 (right panel) mice. The corresponding transgene content (genotype) of the animals is indicated above the images (arrowheads indicate loxP sites; ex 4, exon 4; PV, parvalbumin promoter). In PV-Δγ2 mice the γ2 mRNA signal is lost in areas with a high density of PV-positive cells, e.g., reticular thalamus (rt), colliculi (col), Purkinje cells and molecular layer of the cerebellum (Cb). The autoradiograph on the left was obtained with an oligonucleotide specific for parvalbumin, the autoradiographs in the middle and on the right were obtained with a γ2 (exon 4) -specific oligonucleotide. H, hippocampus. (Scale bar, 2 mm.)

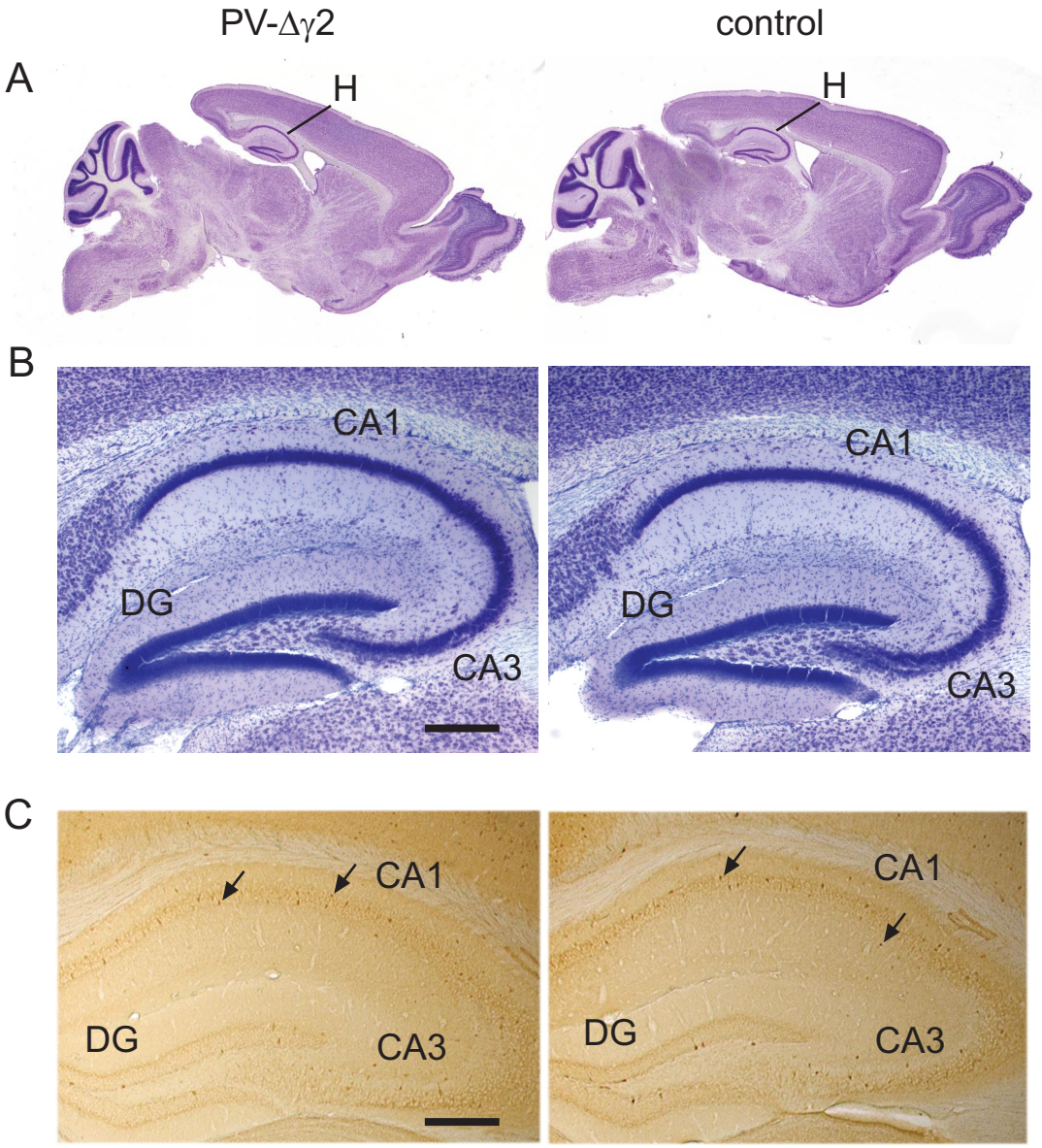

Fig. S2. Adult PV-Δγ2 mice have unaltered brain morphology and show normal distribution and quantity of PV-positive interneurons. (*A* and *B*) Cresyl violet staining of sagittal brain sections from PV-Δγ2 (left) and control (right) mice reveals no difference in brain morphology between the genotypes. (*B*) Higher resolution images of the hippocampus. (*C*) PV immunoreactivity in coronal sections of PV-Δγ2 (left) and control (right) mouse hippocampi shows no differences in number and distribution of PV-positive neurons (arrows). H, hippocampus; DG, dentate gyrus. (Scale bars: *B*, 500 μm; *C*, 350 μm.)

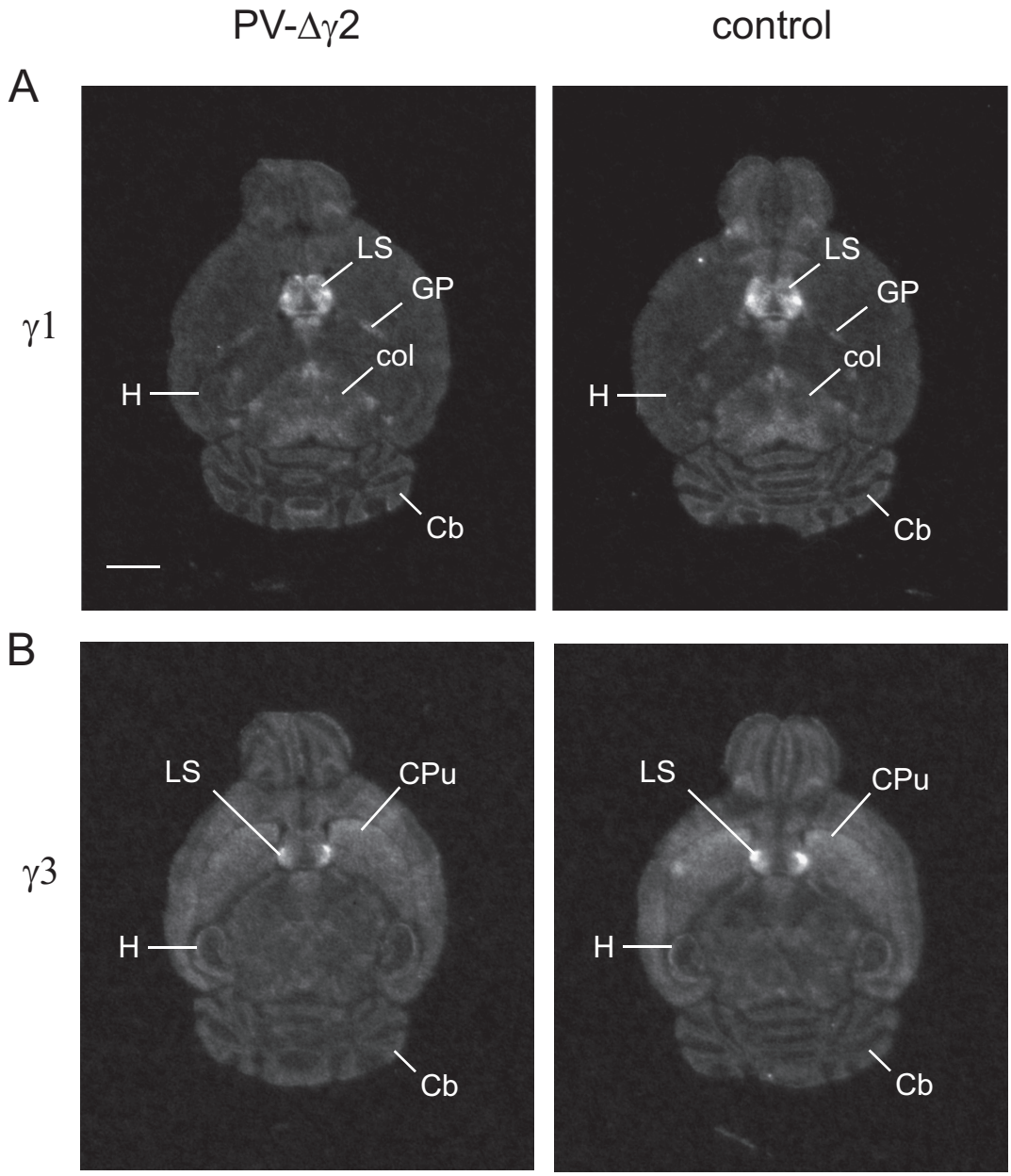

Fig. S3. Transcript levels and distribution of γ1 and γ3 mRNAs are unchanged in PV-Δγ2 mice. In situ hybridization (X-ray film) autoradiographs showing the expression of $GABA_A$ receptor γ1 (*A*) and γ3 (*B*) subunit mRNAs in horizontal brain sections from adult PV-Δγ2 (*Left* in *A* and *B*) and control (*Right* in *A* and *B*) mice. Autoradiographs were obtained with oligonucleotides specific for γ1 (*A*) and γ3 (*B*) mRNA. Cb, cerebellum; col, colliculi; CPu, caudate putamen; GP, globus pallidus; H, hippocampus; LS, lateral septum. (Scale bar, 2 mm.)

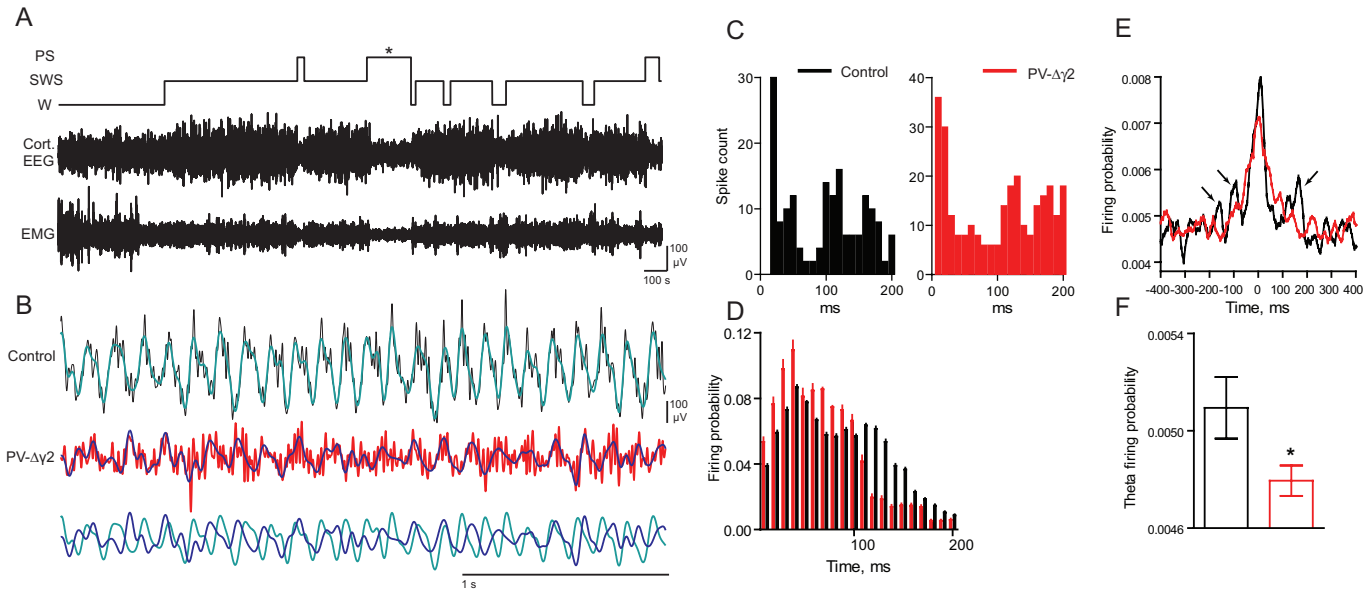

Fig. S4. Representative data examples. (*A*) An example of EMG, neocortical EEG and reconstructed vigilance states (W - waking, SWS - slow-wave sleep, PS - paradoxical sleep) from a PV-Δγ2 mouse. (*B*) Hippocampal EEG recorded during PS (in PV-Δγ2 mouse during an episode marked in (*A*) with an asterisk). Theta rhythmicity is indicated in 1–20 Hz bandpass filtered signals (green and blue traces) superimposed on corresponding 1–85 Hz filtered signals (black and red traces). Bottom traces show normalized 1–20 Hz filtered signals. Note reduced regularity of theta oscillations in the mutant (blue trace). (*C*) Interspike histograms of 2 putative pyramidal cells during theta oscillations. (*D*) Group average of interspike histograms for pyramidal cells during theta oscillations. Spike counts in individual unit histograms are binwise (10 ms bin) normalized by the total number of spikes in a train. (*E*) Average cross-correlations (CCGs) of putative pyramidal cells (157 pairs, control, 313 pairs, PV-Δγ2) obtained from complete recording sessions. Spike counts in each 5 s bin of individual unit CCGs is scaled to total spike count. Arrows indicate theta-band CCG peaks (lags of 100 to 200 ms) in control. (*F*) Group statistics for the theta-band firing probability (mean of the unitwise theta-band average probability ± SEM). *, $P \approx 0.01$. The reduction of short lags (≈50 ms around 0) cofiring in the mutant is not significant. Interspike histograms and cross-correlations of pyramidal cells indicate reduced theta-band rhythmicity of single cells and population discharge respectively.

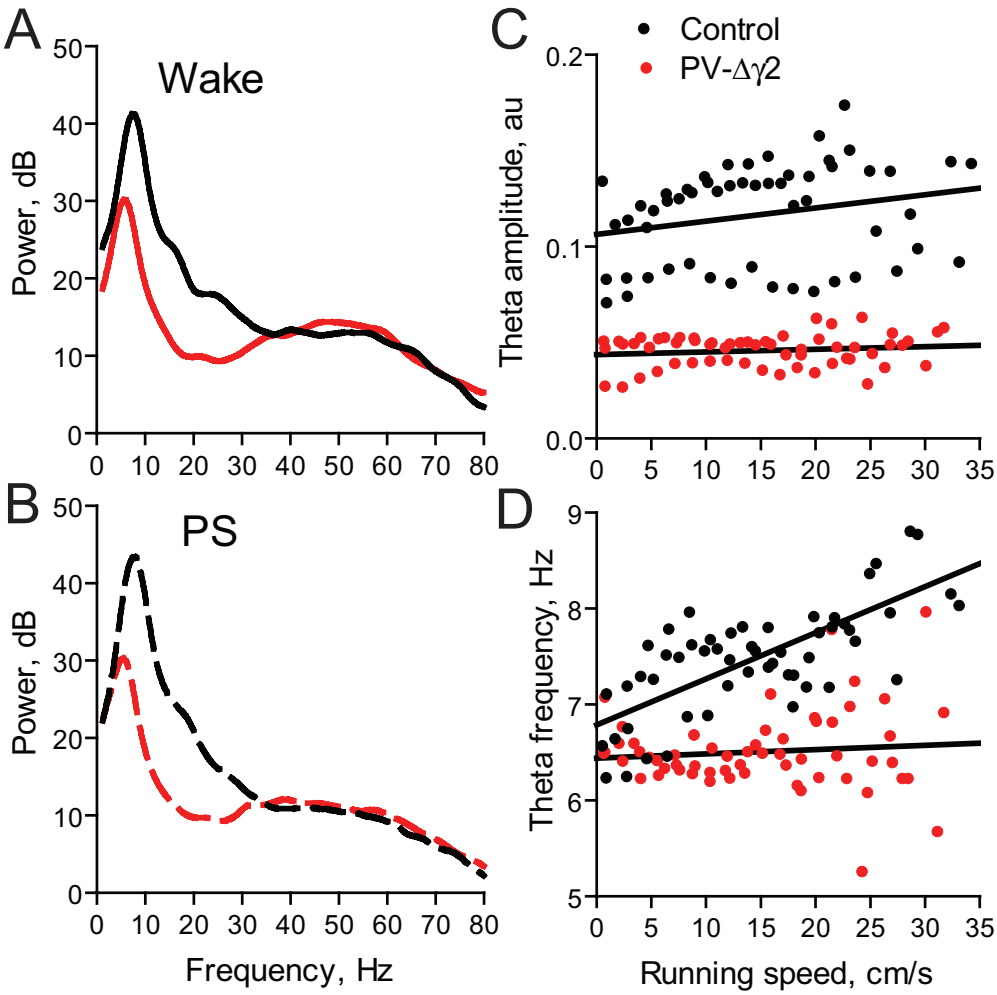

Fig. S5. (*A* and *B*) Log-power spectral density of hippocampal EEG during waking and paradoxical sleep (PS). (*C* and *D*) Association between theta rhythm features and running speed in control and PV-Δγ2 mice. A.u., arbitrary units, Hilbert transformed amplitude of theta LFP (5–10 Hz bandpass).

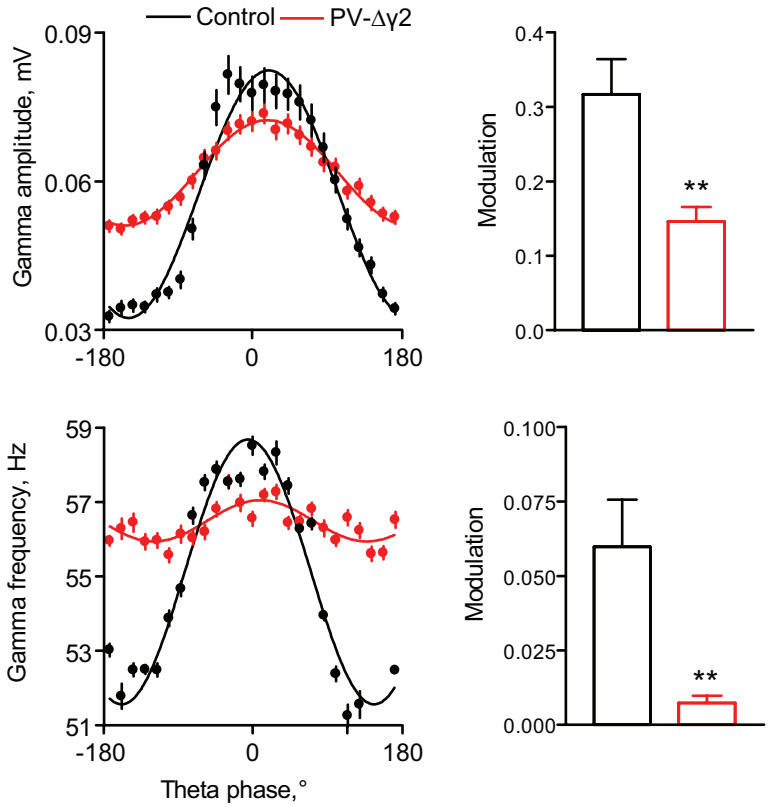

Fig. S6. Uncoupling of theta and gamma oscillations during paradoxical sleep. (*Left*) Altered modulation of gamma amplitude and gamma frequency (mean ± SEM) for all theta oscillation epochs detected during paradoxical sleep. (*Right*) Group statistics of modulation coefficients derived from histograms of part *A*. **, $P < 0.01$.

Other Supporting Information Files

SI Appendix